Influence of dislocation cells on hydrogen embrittlement in wrought and additively manufactured Inconel 718

Check for updates

Claudia-Tatiana Santos Maldonado [1] ✉, Alfredo Zafra[2,3,4], Emilio Martínez Pañeda [2,3], Paul Sandmann[5], Roberto Morana[6] & Minh-Son Pham [1] ✉

Hydrogen embrittlement (HE) is a major issue for the mechanical integrity of high-strength alloys exposed to hydrogen-rich environments, with diffusion and trapping of hydrogen being critical phenomena. Here, the role of microstructure on hydrogen diffusion, trapping and embrittlement in additively manufactured (AM) and wrought Inconel 718 is compared, revealing the key role played by dislocation cells. Trapping behaviour in hydrogen-saturated alloys is analysed by thermal desorption spectroscopy and numerical simulations. A high density of hydrogen traps in cell walls, attributed to dense dislocations and Laves phases, are responsible for the local accumulation of hydrogen, causing significant loss in strength, and triggering cracking along dislocation cell walls. The influential role of dislocation cells alters fracture behaviour from intergranular in the wrought alloy to intragranular for the AM alloy, due to the large proportion of dislocation cells in AM alloys. In addition, the cellular network of dislocations accelerates hydrogen diffusion, enabling faster and deeper penetration of hydrogen in the AM alloy. These results indicate that the higher HE susceptibility of nickel superalloys is intrinsically associated with the interaction of hydrogen with dislocation walls.

The Ni-based superalloy Inconel 718 exhibits outstanding mechanical properties at high temperatures and corrosion resistance in extreme and sour environments, attributed to the precipitation of finely dispersed intermetallic compounds, γ' – Ni3(Ti, Al), and γ'' – Ni3Nb, which are coherent with the FCC γ matrix[1,2] and the presence of Cr in its elemental composition. These features make Inconel 718 a suitable candidate for a range of applications in aerospace and energy, including power generation, gas, and oil industries[3–6]. In such applications, components often require highly complex geometries, which are difficult to achieve through subtractive manufacturing routes due to the high strength and low thermal conductivity of the alloy[7,8]. Alternative fabrication processes, such as Additive Manufacturing (AM), have gained popularity for Inconel 718 components[9–11], with Laser Powder Bed Fusion (LPBF) being a commonly used AM process due to its ability to generate complex geometries. However, AM involves extremely high thermal gradients, rapid cooling rates, and repeated thermal cycles, leading to unique microstructures and components exhibiting properties distinct from conventionally manufactured counterparts[12,13].

As AM techniques have gained popularity in the manufacturing of Ni-based superalloys, the relationship between processing parameters (laser power, scan speed, hatch distance, layer thickness, and scanning strategy) and consolidation density, microstructure, and mechanical properties has been of considerable interest to optimise builds[7,13–19]. However, Ni-based superalloys are often intended for critical applications involving direct contact with hydrogen-rich environments during production, storage, transportation, or service, such as exposure to high-pressure hydrogen gas or corrosive environments. This exposure can lead to hydrogen uptake and premature alloy failure due to hydrogen embrittlement (HE), a phenomenon widely observed in conventionally manufactured Ni-based superalloys[20–22]. HE is caused by the absorption and diffusion of hydrogen atoms into the metal lattice and subsequent segregation in microstructural defects, which degrades the mechanical properties of the material when a load is applied[23,24]. The effects of hydrogen in wrought Ni-based alloys have been documented since the mid-1980s, with particular emphasis on the correlation between their stress corrosion cracking susceptibility with their microstructure[3,5,6,25–29] and failure mechanisms[3,6,28,30–32]. The two major HE mechanisms driving the failure in Ni-based superalloys are hydrogen-enhanced decohesion (HEDE)[24,33,34] and hydrogen-enhanced localised plasticity (HELP)[23,33]. The former assumes that the accumulation of a critical

[1]Department of Materials Science, Imperial College London, Exhibition Road, London, SW7 2AZ, UK. [2]Department of Civil and Environmental Engineering, Imperial College London, London, SW7 2AZ, UK. [3]Department of Engineering Science, University of Oxford, Oxford, OX1 3PJ, UK. [4]Department of Materials Science, University of Oviedo, 33203 Gijón, Spain. [5]Mechanical Engineering, Imperial College London, London, SW7 2AZ, UK. [6]BP Exploration Operating Company Limited, Chertsey Road, Sunbury-on-Thames, TW16 7LN, UK. ✉e-mail: c.santos-maldonado19@imperial.ac.uk; son.pham@imperial.ac.uk

amount of hydrogen at microstructure sites, such as grain boundaries or matrix/precipitates interfaces, decreases the cohesive strength of the metallic atom bonds and triggers interface decohesion at such locations[28,35,36]. On the other hand, the HELP mechanism suggests that hydrogen atoms increase dislocation mobility (by reducing the Peierls stress for dislocation movement), and the subsequent pile-up enhances the localised plasticity, facilitating shear failure along slip planes [37].

With hydrogen becoming increasingly recognized as a future sustainable energy vector and AM materials being increasingly used, it is expected that the exposure of AM Ni-based superalloys to hydrogen-rich environments will rise considerably. Thus, an in-depth understanding of hydrogen embrittlement in alloys is necessary to prevent hydrogen-induced catastrophic failures. While a number of studies have been conducted on the HE of Ni-based superalloys produced by wrought and other processes, limited research has been conducted on Ni-based AM components[38–44]. Among these studies, a majority focused on the effect of hydrogen on the mechanical properties and fracture behaviour of AM Inconel 718[38–44]. For example, Hesketh et al.[41] showed the mechanical degradation of AM builds with emphasis on the printing direction (vertical or horizontal), whilst Li et al.[37] suggest that HE in AM Inconel 718 occurs along the γ/Laves interface. Despite recent studies suggesting that hydrogen embrittlement in AM components is related to cellular dendritic boundaries containing dense dislocations (i.e., dislocation cells)[42–44], comprehensive studies on the detailed correlation of microstructure with hydrogen absorption, diffusivity, crack initiation and hydrogen embrittlement are still missing. In particular, the direct influence of dislocation cells on crack initiation has not been reported for hydrogen-exposed AM alloys. Furthermore, there is a need for (1) a hydrogen trapping assessment in fully saturated samples to gain insight into the nature of the preferential trapping sites that influence crack initiation and propagation; and (2) a hydrogen diffusivity and uptake assessment for samples with the same thickness as for tensile tests, which will enable correlating HE susceptibility indexes to hydrogen content. Recently Maksimkin et al.[45]. provided a hydrogen diffusivity value in annealed samples based on gas permeation studies. However, such studies are time-consuming and challenging to perform. To overcome the limitations associated with gas permeation, an approach based on isothermal Thermal Desorption Spectroscopy (ITDS) is presented here.

Thus, there is a need to address the aforementioned gaps and examine the effect of the microstructure (in particular dislocation cells) on hydrogen embrittlement, correlating the microstructure with the hydrogen absorption, diffusion, and hydrogen trapping and embrittlement behaviour. Consequently, the present study comprehensively examines the microstructure of AM compared to a wrought condition to investigate the role of dislocation cells on hydrogen embrittlement. The hydrogen absorption and the corresponding mechanical behaviour of the wrought and AM Inconel 718 are quantified by considering different durations of hydrogen charging needed to achieve a fully charged condition. This enabled reliable quantification of hydrogen diffusivity in wrought and AM using isothermal desorption analysis (ITDS) and a hydrogen trapping assessment in fully saturated specimens. Through this method, the mechanical performance can be correlated with the hydrogen content (as opposed to specific charging characteristics). Numerical analyses were used complementary with the TDS measurement to quantitatively characterise the hydrogen diffusivity. Such detailed examinations provide valuable insights into the role of microstructure (in particular dislocation cells) on hydrogen absorption, diffusion, trapping, and fracture behaviour, shedding light on the mechanisms responsible for the hydrogen embrittlement in Inconel 718.

Results
Microstructure conditions
As-received wrought Inconel 718 showed equiaxed grain morphology (an average grain size of 6.2 μm) with dominant Σ3 annealing twins (Fig. 1a), indicating that the annealing heat treatment was performed for the wrought condition. Pole figures (Fig. 1g) showed a slight texture orientation in the rolling direction. In contrast to the wrought condition, AM Inconel 718 (Fig. 1b) consisted of coarse columnar grains along the BD separated with slender grains which appeared to be equiaxed in their cross-section view (Fig. 1c). The columnar microstructure is the result of the epitaxial growth
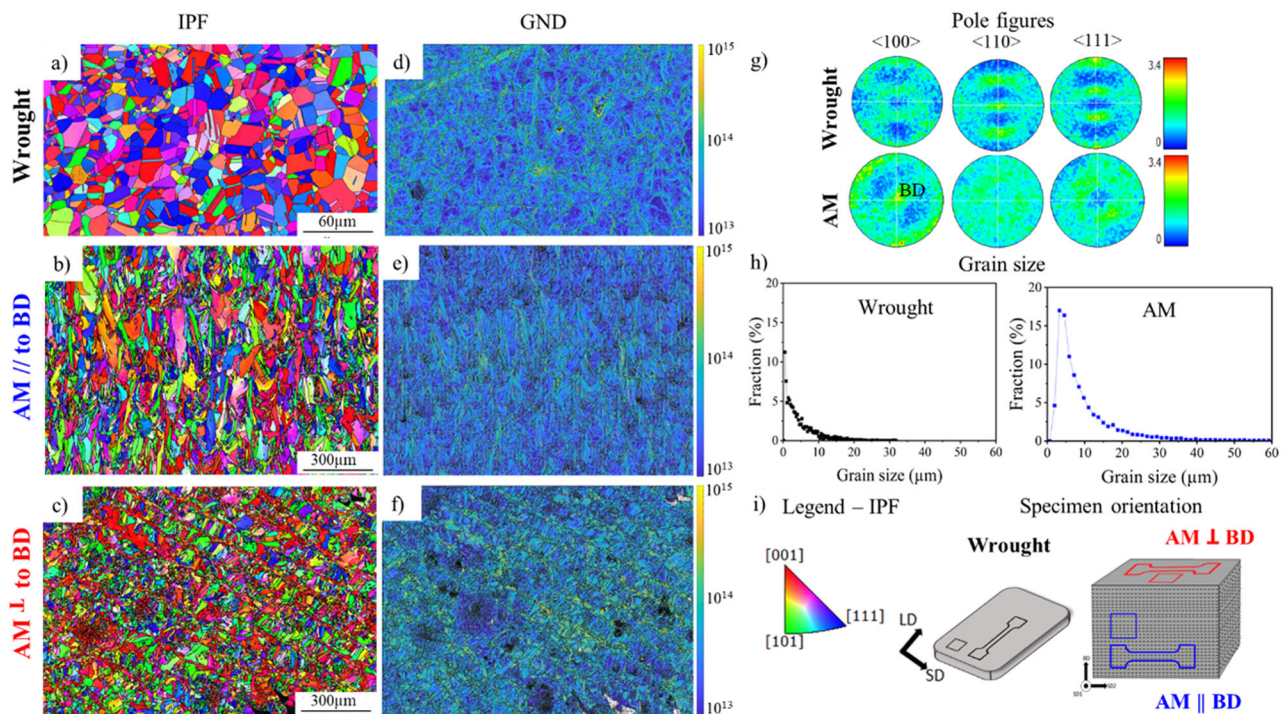

Fig. 1 | Microstructure of the wrought and AM conditions of Inconel 718. **a–c** Inverse pole figure (IPF) maps along the build direction and perpendicular to the build direction, (**d–f**) geometrically necessary dislocation (GND) maps, (**g**) pole figures from wrought and AM, (**h**) average grain size analysis, and (**i**) legend and specimen orientation is shown as a reference, LD long direction and SD short direction of the as-received sheet, AM ‖: sections parallel to the building direction, and AM⊥: sections perpendicular to building direction.

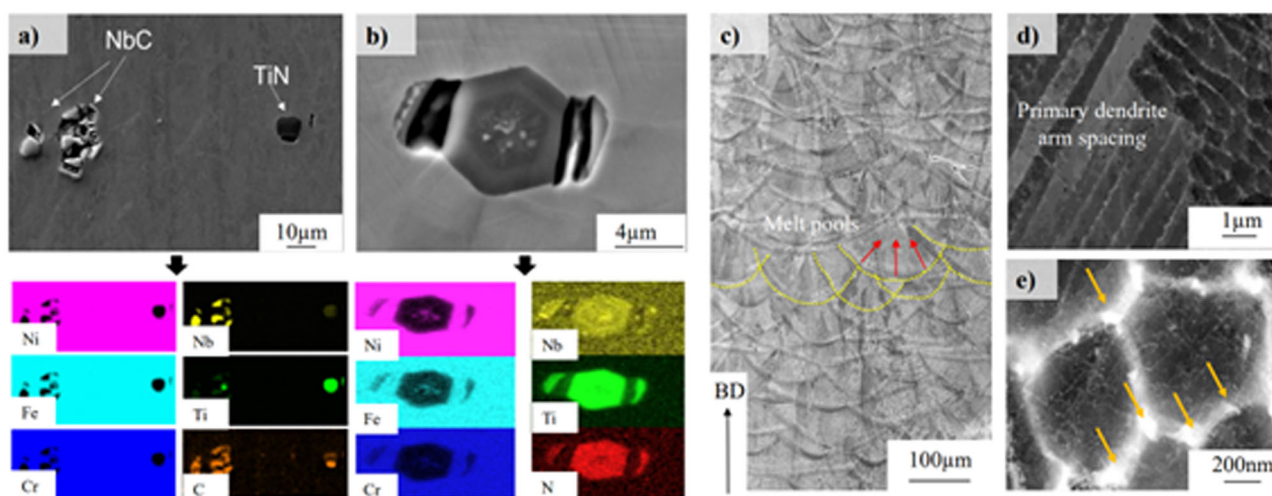**Fig. 2 | Microstructure of wrought Inconel 718.** Microstructure of wrought Inconel 718 showing intermetallic compounds of (**a**) irregular (Nb,Ti)C carbides and (**b**) hexagonal (Ti,Nb)N precipitates accompanied by the EDS maps (same scale bar). The Microstructure of AM Inconel 718 ∥ to BD is shown from (**c**–**e**), where (**c**) fish- scale patterns along the building direction can be seen (melt pools are highlighted in yellow). Cellular dendrites are observed (**d**) parallel and (**e**) perpendicular to the plane of view, containing dense dislocations (white curve lines) with Laves phases indicated with orange arrows.

occurring during the deposition of successive layers and the slender grains were found to be along the centre of deposition track[46]. The AM condition has a preferred crystallographic texture with a < 100 > direction aligned with the BD, as evidenced by the pole figures shown in Fig. 1g. The average grain size, calculated from both the AM⊥ and AM∥ observations, is 13.9 μm. Similar microstructural characteristics have been previously documented in AM components[46–49]. The geometrically necessary dislocation (GND) maps (Fig. 1d–f) suggest a higher dislocation density in the fine slender grains of the AM condition. These slender grains were located along the centre of the melt track, which is usually the last region to solidify. Hence, grains in this region are more strained and contain a higher number of dislocations. On the contrary, the lower intensity of the GND map obtained in the wrought condition revealed a lower dislocation density. To capture the great GNDs difference between wrought and AM a much higher magnification is necessary. Al-Lami et al.[50] performed a quantitative analysis of the geometrically necessary dislocations (GNDs) of AM Inconel 718, and correlated it with the microstructure, concluding that the fine equiaxed grains contained a high GNDs density.

EDS elemental mapping of the wrought Inconel 718 revealed Ti-rich and Nb/Ti-rich carbo-nitrides (Fig. 2a, b). Carbides were irregular, while nitrides displayed a characteristic hexagonal shape. In addition, SEM imaging of etched surfaces of AM ∥ to BD (Fig. 2c) shows a fish-scale pattern consisting of arc-shaped weld beads. Selected fusion boundaries are highlighted in yellow for reference (Fig. 2c). High magnification SEM reveals a fine cellular (or cellular dendritic) microstructure within melt pools, with such a cellular microstructure being characteristic of AM processes[14,47,51,52]. The cellular dendrites, shown in Fig. 2d, e, exhibit an average spacing of 0.55 nm, which is consistent with the literature[11,19,53–55], and are characterized by dense dislocation tangles at the cellular boundaries (Fig. 2e) caused by the high thermal stresses and thermal cycles during printing[56–58]. Laves phase particles were also observed (appearing white in Fig. 2e and indicated with yellow arrows) at the cell boundaries. Porosity quantification was conducted on all the tensile specimens of the AM condition, showing the consolidation with an average density of 99.8% and 99.7% for AM ∥ and AM⊥ samples, respectively.

Hydrogen absorption and trapping

The total hydrogen content measured for different charging times at 90 °C for the wrought and AM Inconel 718 is shown in Fig. 3a. To provide statistically representative data on hydrogen absorption, around 30 wrought and 40 AM specimens were evaluated, and the average value is reported in Fig. 3a with the error bar representing the calculated standard deviation. For example, Fig. 3b shows the TDS desorption profiles (wppm/s vs temperature) of AM ∥ for different charging times.

Figure 3a shows a considerably higher hydrogen uptake in the AM microstructure (around 1.5 times higher) than wrought Inconel 718. The average hydrogen content for long charging times was ≈150 wppm for the wrought and ≈200 wppm for AM ∥ and AM ⊥. Differences in hydrogen contents between AM samples of directions parallel and perpendicular to the BD are negligible and can be attributed to data variability (error bars always overlap between AM ∥ and AM ⊥). A concentration plateau was achieved after approximately 7 days of charging for all the conditions. This fact is confirmed by the evolution of the shape of the TDS profiles corresponding to AM ∥ and shown in Fig. 3b. A single-peak desorption profile is only attained for charging times over 4 days. Therefore, a hydrogen trapping assessment of wrought and AM Inconel 718 was conducted only on samples charged for 7 days or longer, which, according to Fig. 3, had attained a uniform hydrogen concentration across their thickness. This condition becomes particularly relevant for applying trapping models such as Oriani's[34] or McNabb-Foster's[59], which allow the determination of the trap binding energy, E_b, and the trap density, N_t. In this work, E_b and N_t were estimated by fitting the output of numerical TDS experiments based on Oriani's trapping model—which assumes local equilibrium between hydrogen in the lattice and microstructural sites – to the experimental TDS desorption curves using the Matlab App *TDS Simulator*[60]. This procedure allows for trapping characterisation without the need to perform TDS experiments at different heating rates, as typically adopted when using the so-called Kissinger or Choo-Lee method[61]. It should be noted that the applicability of Kissinger's approach using different heating rates has been reported to be inadequate to characterise trapping in lattice diffusion-dominated metals, such as FCC crystal structures like Ni-based alloys and austenitic steels[62–64],

Figure 4 shows an example of such a fitting conducted on experimental TDS curves (14 days of charging) employing Oriani's model upon the assumption of 2 types of trapping sites. In addition, the average E_b and N_t values of each trap type for the wrought and AM conditions are gathered in Table 1. E_b represents the interaction or trap binding energy between hydrogen atoms and microstructure traps, and is calculated as $E_b = E_a - E_L$, where E_a is the activation energy of hydrogen for a given type of trap, and E_L is the activation energy of hydrogen diffusion in the lattice (a value of ~39 kJ/
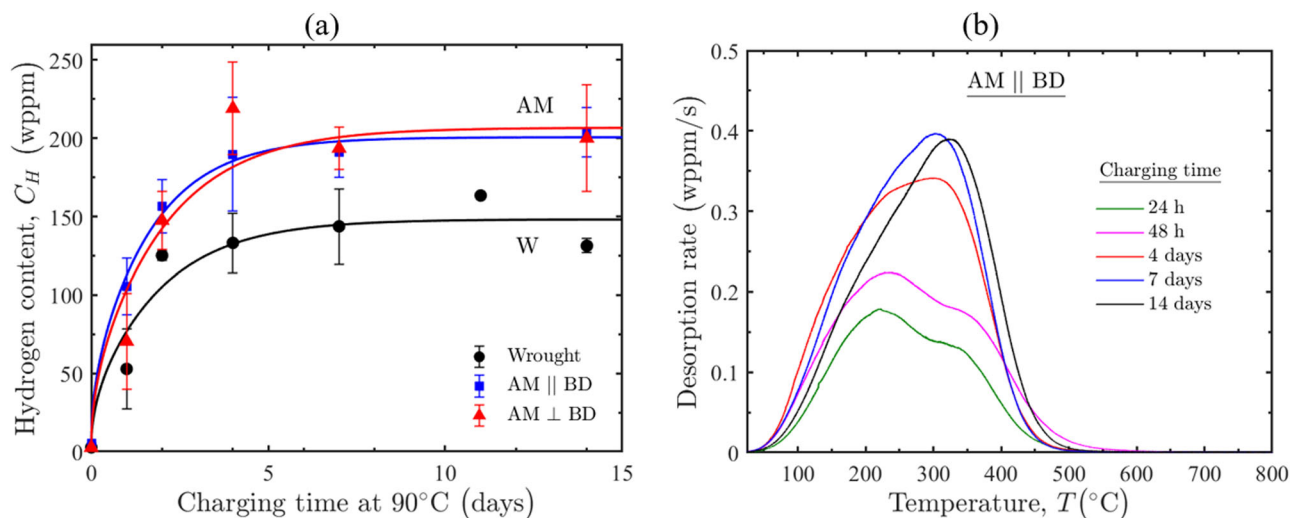
Fig. 3 | Hydrogen Content and desorption profile. a Total hydrogen content vs. charging time for the wrought, AM ‖ and AM ⊥ condition and (**b**) characteristic TDS desorption profiles of AM ‖ for different charging times.
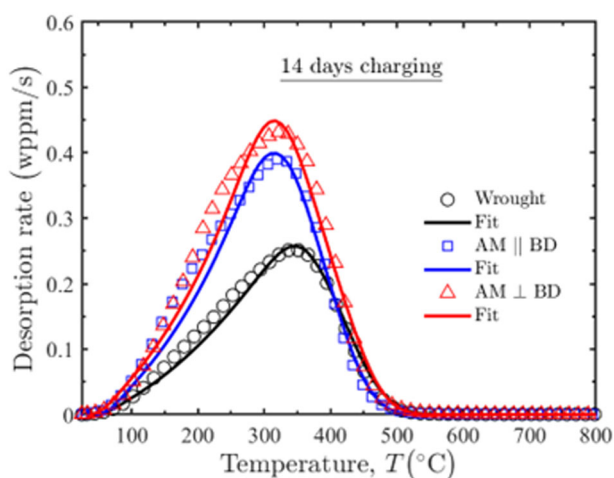

Fig. 4 | TDS numerical fitting for trapping analysis. Fitting of Oriani's model (2 trapping sites) to experimental TDS curves for wrought and AM Inconel 718 charged for 14 days.

Table 1 | Average binding energies, E_b, and densities, N_t, of the two main trapping sites of Wrought and AM Inconel 718

Condition	Trap 1		Trap 2	
	E_b [kJ/mol]	N_t [traps/m³]	E_b [kJ/mol]	N_t [traps/m³]
Wrought	7.8	2.5×10^{26}	30.7	1.5×10^{26}
AM ‖	5.0	7.0×10^{26}	26.5	4.0×10^{26}
AM ⊥	4.2	5.5×10^{26}	27.7	6.0×10^{26}

Table 2 | Hydrogen diffusivity, D, determined through Isothermal TDS at different temperatures for wrought, AM ‖ and AML

	Diffusivity, D (m²/s)	
T (ºC)	Wrought	AM ‖
22	$2.59 \pm 0.76 \times 10^{-15}$	$4.22 \pm 0.71 \times 10^{-15}$
90	$2.14 \pm 0.09 \times 10^{-13}$	$3.00 \pm 0.43 \times 10^{-13}$
200	$9.25 \pm 0.18 \times 10^{-12}$	9.52×10^{-12}
300	4.74×10^{-11}	6.47×10^{-11}
400	$2.38 \pm 0.24 \times 10^{-10}$	$1.50 \pm 0.04 \times 10^{-10}$

mol can be used for pure Ni[65,66]. Apart from the differences in hydrogen contents between wrought and AM conditions, already discussed in the context of Fig. 3, it is worth noting that the main peak in the TDS output of the wrought is shifted to a slightly higher temperature than the AM TDS curves. Moreover, while the binding energy of both lattice and microstructure sites is higher in the wrought than in the AM condition, the trap density is considerably higher in the AM condition (both along and perpendicular to the BD) than in the wrought (Table 1).

Hydrogen diffusion

Hydrogen diffusivity, D, was determined in the wrought and AM Inconel 718 using isothermal TDS experiments conducted at 22, 90, 200, 300 and 400 °C on samples pre-charged for more than 7 days. The hydrogen desorption rate (wppm/s) versus time was monitored during a certain time at the targeted temperature, and the output of a 1-D hydrogen transport COMSOL simulation was fitted to the experimental data following a parameter optimization procedure developed in Matlab[67,68]. Table 2 shows the average diffusivity (± standard deviation) obtained in all the isothermal TDS experiments conducted for the wrought and AM conditions (note that the AM ‖ was selected as the representative for the AM condition because the

difference between ‖ and ⊥ was negligible, as mentioned earlier). As an example, Fig. 5a, b shows the fitted experimental curves for ITDS experiments performed at 22 and 90 °C in the wrought and AM conditions.

Firstly, it is worth noting that FE calculations produce an excellent fit for all the experimental data across the tested temperatures, with coefficients of determination (R^2) that were consistently higher than 0.95. Secondly, the amount of desorbed hydrogen for a certain period of time (area below the curve) is considerably higher in both AM conditions, which confirms the higher hydrogen concentration present in these conditions after hydrogen charging (i.e., higher absorption capacity) in line with the results reported in Fig. 3a. Finally, the hydrogen diffusivity was higher in the AM conditions, which was especially noticeable at low temperatures, i.e., RT and 90 °C, where trapping effects are more pronounced. It is noteworthy that the diffusivity measured in AM ⊥ was lower than in AM ‖. Nevertheless, the hydrogen absorption and diffusivity differences between AM ‖ and AM ⊥ were negligible.
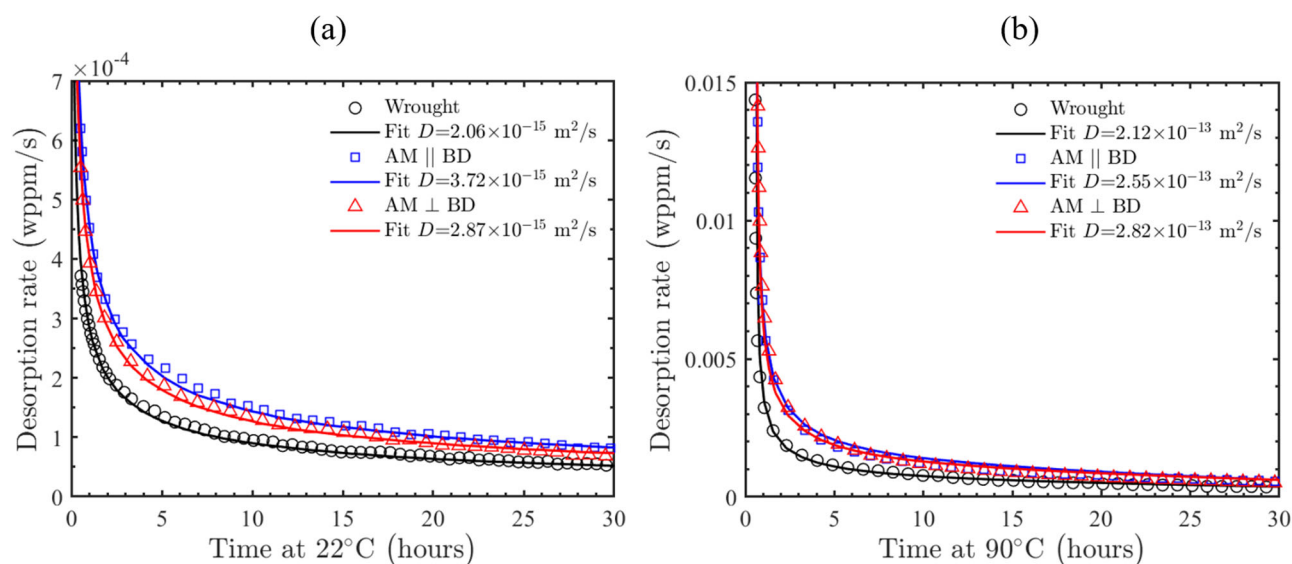
Fig. 5 | Isothermal TDS and numerical fitting for diffusivity calculations. Isothermal TDS (ITDS) experiments performed at (**a**) 22 °C and (**b**) 90 °C and the best fit to 1-D hydrogen transport FE simulations.

The diffusivity calculated from ITDS results shows a good agreement with literature values of wrought Inconel 718 for different metallurgical conditions[45,66], as shown in Fig. 6 and Table 3. Data obtained for the AM || condition (Table 2) was used to identify the values of the D_0 and E_a for the Arrhenius equation at various temperatures. Although diffusivity values for AM Inconel 718 at different temperatures are scarce, the data set presented in this paper aligns with the results of Maksimkin et al.[45] who performed a gas permeation test in annealed AM Inconel 718[45]. Minor discrepancies between the present results and the aforementioned ones can be associated with metallurgical differences and the use of different testing methodologies (i.e., the use of isothermal TDS vs. gas permeation experiments in the Maksimkin's et al.[45]).

Hydrogen embrittlement (HE)
Slow strain rate testing (SSRT) was performed on the wrought and AM Inconel 718 samples with and without hydrogen pre-charging. The stress-strain engineering curves are presented in Fig. 7, and the average tensile properties (σUTS and reduction of area (RA)) are provided in Table 4, along with the corresponding hydrogen embrittlement indexes (HEI), as defined in Section 2.5, which represent a valuable indicator to assess the impact of hydrogen on the mechanical properties.

In the non-charged condition, AM specimens exhibited higher yield strength and σ_{UTS} than wrought samples. However, the ductility, as indicated by the final elongation and RA, was lower in AM specimens. After hydrogen charging, the ductility significantly decreased in all samples compared to the non-charged conditions. Notable differences were observed between the wrought and AM Inconel 718. While the wrought condition still exhibited some ductility even after >7 days of charging (with a reduction in final elongation from 35% down to about 5%), a profound decrease in ductility is evident in the AM samples. After only 4 days of charging, the samples fail in a brittle manner at values ranging around the yield stress, suggesting a more significant influence of hydrogen on the mechanical behaviour of the AM condition. The reduction in area followed a similar trend, with hydrogen embrittlement indexes ranging from 50% to 60% for the wrought condition and 60% to 70% for the AM condition.

Micrographs of fracture surfaces and sections parallel to the loading direction for the wrought and AM conditions are shown in Figs. 8, 9, respectively. For the non-charged samples, both the wrought (Fig. 8a) and AM (Fig. 9a) conditions exhibited significant necking prior to failure. Slip traces were abundantly seen in the gauge region, and the fracture surface was characterised by dimple features (Fig. 8a), suggesting ductile fracture behaviour. In contrast, pre-charged hydrogen samples demonstrated very
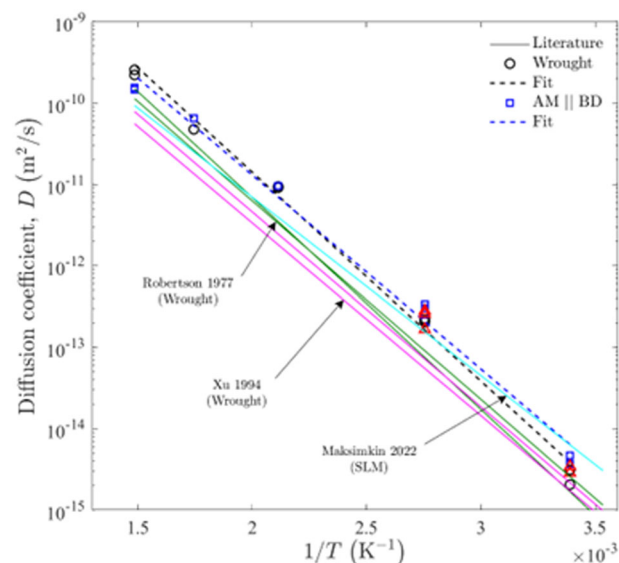

Fig. 6 | Hydrogen diffusivity at different temperatures of wrought and AM Inconel 718. Dashed lines in the plot represent a fit of wrought and AM || datasets to the Arrhenius relationship $D = D_0 exp(-E_a/T)$; where D_0 and E_a are the pre-exponential factor and activation energies for diffusion, respectively. Solid lines correspond to the studies performed within different Temperature ranges by Robertson[66] in green, Xu et al.[95] in pink, and Maksimkin et al.[45] in blue.

little necking, suggesting a significant loss (of ductility) consistent with the ductility loss seen in the stress-strain curve (Fig. 7). Fracture surface observation shows a brittle fracture manner, in particular for a longer duration of hydrogen charging. In the case of the wrought condition, for short charging times (24 h), brittle and intergranular (IG) fracture was dominantly observed at the sample outer regions. However, ductile dimples were still seen in the centre of fractured samples, suggesting hydrogen did not diffuse deep into the centre of the samples. With increasing the charging time, consistent with the hydrogen absorption shown in Fig. 3, hydrogen penetration increased, leading to a larger area of brittle fracture. After 4 days of charging, the hydrogen-induced brittle fracture regions exceeded 60%, with some isolated regions remaining ductile. Following 14 days of charging, the entire sample displayed brittle intergranular characteristics, indicating that a uniform hydrogen distribution was achieved (Fig. 8b).

Table 3 | Comparison within the literature of the H diffusivity calculated with gas permeation experiments and ITDS analysis results

Ref.	Alloy	Condition	D_0 (m²/s)	E_a (kJ/mol)	T_{range} (°C)	Method
Robertson[66]	718	Cold-rolled ST: 954°C/1h +AC ST:1038°C/1h +AC	4.70×10^{-7} 1.10×10^{-6} 1.10×10^{-6}	46.65 49.79 50.00	150–500	Gas Permeation (0.1–0.3 MPa)
Xu et al.[95]	718	Cold-rolled ST: 980°C/2h +AC	2.82×10^{-7} 1.82×10^{-7}	45.82 45.30	210–430	Gas Permeation (0.1 MPa)
Maksimkin et al.[45]	718	SLM+A: 750°C/2.5h	1.66×10^{-7}	41.90	282–727	Gas Permeation (0.9 MPa)
This work	718	Wrought LPBF AM ∥	1.91×10^{-6} 7.51×10^{-7}	49.10 45.57	22–400	Isothermal TDS

The value of D_0 obtained are very similar to those found in literature, suggesting the ITDS technique a reliable method for calculating hydrogen diffusivity. ST corresponds to Solution treated, AC to Air cooling, SLM to Selective Laser Melting, A to Annealing and LPBF to laser powder bed fusion.
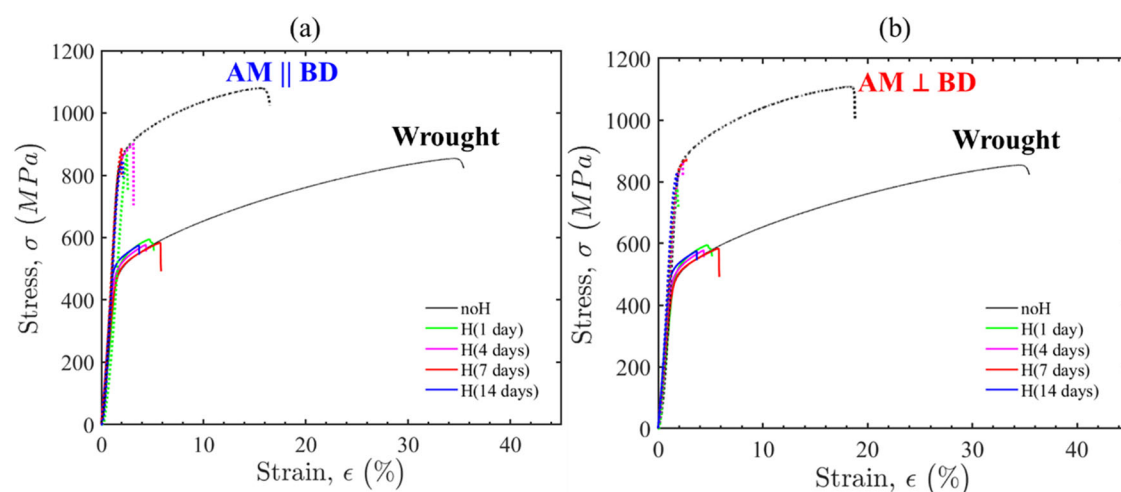

Fig. 7 | Tensile behaviour of non-charged and H-charged wrought and AM Inconel 718. Stress-Strain uniaxial tension behaviour of Inconel 718 for the (**a**) wrought and AM ∥ BD (**b**) wrought and AM ⊥ BD for the non-charge and H-charged conditions. H-charging duration was 1, 4, 7, and 14 days.

Although the stress-strain behaviour of the AM specimens exhibited a more significant reduction in ductility compared to the wrought specimens, the fracture surface of the AM appeared not intergranular as observed in the wrought Inconel 718 (Fig. 9). The fracture surface of AM specimens after 14 days was intragranular, and resembled the cellular microstructure (Fig. 9b), suggesting that cracks initiated and subsequently propagated along cellular boundaries.

Discussion

The characteristic fine cellular microstructure in AM builds (Fig. 2c–e) is found to result in a higher strength. The boundaries between cells contain dense dislocations, Laves phase and carbides. It has been shown that dislocations at cellular boundaries provide effective resistance to the motion of mobile dislocations, significantly increasing the strength of AM alloys without compromising the ductility[69,70].

While the cellular microstructure provides high strength and good ductility, this study shows that it has a profound impact on hydrogen diffusivity, trapping and absorption. In particular, the hydrogen absorption capacity of AM builds was about 1.5 times higher than the wrought counterpart, Fig. 3. The high hydrogen concentration stems from a higher density of trapping sites available in the AM condition, as confirmed by the analysis of TDS spectra (Fig. 4 and Table 1). Dislocations are known to be effective trapping sites for hydrogen[71], whilst Laves phases might act as preferential trapping sites due to their high content of Nb, as Nb has been shown to have a high affinity to hydrogen[72]. Therefore, the dense dislocations and Laves phases that were found at the cellular boundaries in the AM condition (Fig. 2e) acted as trapping sites for hydrogen, leading to a high hydrogen absorption in the AM condition. Further research on the effect of the Laves phases on hydrogen trapping is being investigated. In addition, hydrogen can also be trapped at grain boundaries. However, the fact that cracks initiated at the cell boundaries could potentially suggest that dislocation cells are more effective in trapping hydrogen. In the wrought material (where dislocation cells are not present), hydrogen is likely trapped at other microstructural features such as grain boundaries, and the interfaces between the matrix and carbides and nitrides, as reported in the literature[71–73]. While the wrought sample contained finer grains, the dislocation density was much lower than in the AM condition, explaining the lower hydrogen absorption capacity of the wrought condition. The lower density of trapping sites in the wrought (Table 1) suggests that the cellular microstructure in the AM condition is a substantially more effective trapping site than the grain boundaries.

The first TDS peak of both wrought and AM Inconel 718 is attributed to the solubility of hydrogen in lattice interstices[74]. A more energetic second trap type (i.e., Trap 2) is associated with stronger trapping sites that can be grain boundaries, dislocation cells, and interfaces between matrix and particles[20,61]. For example, Lu et al.[74] recently reported similar values on a hydrogen traps analysis performed in a nickel alloy 625 in where two types of peaks were reported with a second peak of high trapping energy (E_b = 24.8–27.13 kJ/mol) corresponding to grain boundaries and dislocations at incoherent interfaces. Therefore, for wrought, the Trap 2 type can be

associated to grain boundaries and carbide-nitrides/matrix interfaces as they are the primary microstructure seen in this condition (Figs. 1, 2). Indeed, it has been reported in a wrought Ni-based alloy that the trapping energy of carbide-type traps is between 20 and 55 kJ/mol[43,75], consistent with the identified values of the E_b of the second type of trapping, 30.7 kJ/mol (Table 2). For the AM condition, the second trap (E_b = 26-28 kJ/mol) may correspond to the hydrogen trapped at the dislocation cells, Laves phase and grain boundaries. In addition, there is chemical segregation towards cell boundaries. The enrichment of Nb, Ti, and Mo might also affect hydrogen trapping; hence, there is a higher susceptibility to hydrogen embrittlement in the AM Inconel 718. Some recent studies of hydrogen embrittlement in AM austenitic stainless steels show that chemical inhomogeneity also affects hydrogen embrittlement[76–78]. In addition, they show different HE behaviour than Inconel 718, with improved/similar resistance to hydrogen than

conventionally manufactured stainless steel. The diffusion of hydrogen takes place via lattice and microstructure features. Not only are dislocations effective trapping sites, but they can also act as fast pathways for hydrogen diffusion (i.e., pipe diffusion)[79], accelerating hydrogen diffusion along dislocation cores. Networks of dislocations can enable deeper penetration of hydrogen into the bulk of samples. Fast diffusion along dislocations at grain boundaries (i.e. short circuits) is well-reported[80]. As the grain size is smaller in the wrought condition (Fig. 1g), the hydrogen diffusion in the wrought is expected to be higher. However, the AM sample contained dense and fine cellular networks of dislocations that considerably enhanced the hydrogen diffusivity (therefore the hydrogen penetration), explaining why faster hydrogen charging was observed for the AM condition, as shown in Figs. 3 and 5, and Table 2. Similar behaviour has been reported in AM 316 L, in which higher diffusivity was attributed to dislocations acting as fast pathways along cell boundaries[81].

Both the AM and wrought samples show a significant reduction in ductility and a shift from ductile to brittle fracture behaviour after hydrogen charging, consistent with the literature[26,27,40,41,43,44,82–87]. The difference in fracture behaviour of the wrought versus the AM condition of the same alloy (i.e., Inconel 718) emphasises the influential role of dislocation cells. The intergranular fracture in the wrought condition highlights the ability of grain boundaries (GBs) to trap hydrogen[31,88–90]. The hydrogen trapping at GBs lowers the local cohesive strength, causing decohesion at these interfaces. In addition, wrought samples also showed that carbides were present at GBs. Figure 10b, c shows carbides at GBs that appeared to be fractured, suggesting that hydrogen was trapped in the carbides (or at the carbide/matrix interface) and caused carbide fracture, contributing to the initiation and propagation of cracks along GBs. Figure 10e is a schematic diagram illustrating the hydrogen trapping at GBs and carbides and decohesion at GBs, causing the intergranular fracture observed in the wrought condition.

Figure 9 suggests that the presence of cellular microstructure in the AM builds changed the fracture behaviour due to hydrogen embrittlement of Inconel 718 from intergranular to intragranular. It is necessary to clarify that a single AM grain contains several cell dendrites. Thus, the fracture is determined to be intragranular. As discussed earlier in Section 4.1, the cellular microstructure of dense dislocations and Laves increased the diffusion and absorption of hydrogen in the AM condition. While trap type 1 of hydrogen is associated with the lattice interstices, trap type 2 (second peak of TDS profile) is likely related to dense dislocations, Laves, and grain boundaries, as discussed earlier. The high concentration of hydrogen along the inter-cellular boundaries lowered the cohesive strength of cell boundaries, causing crack initiation as an intragranular fracture in the AM condition. Figure 11a clearly shows that micro-cracks initiated along a
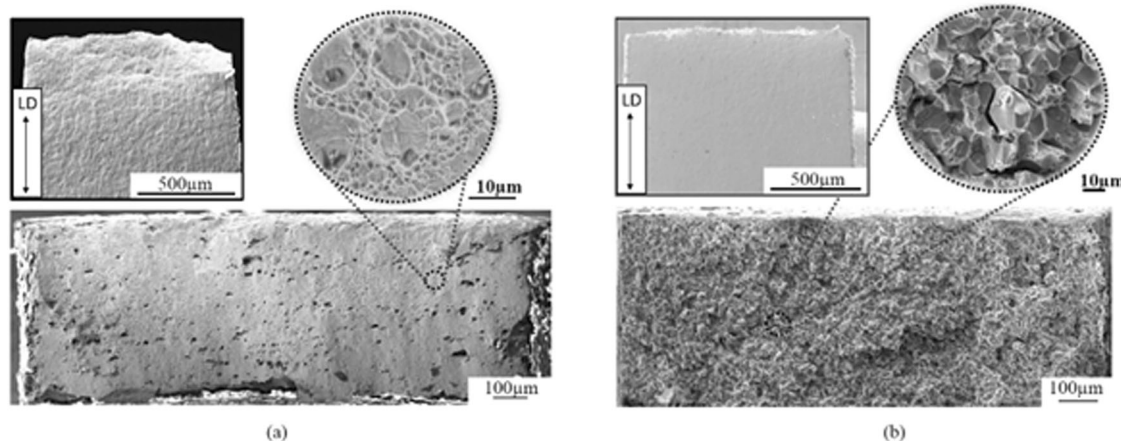
Table 4 | Tensile properties of Inconel 718 - wrought and AM in the two building directions - within different charging times (hydrogen contents)

Inconel 718	Charging time (days)	C_H (wppm)	σ_{UTS} (MPa)	RA (%)	HEI$_{\sigma UTS}$ (%)	HEI$_{RA}$ (%)
Wrought	0	2.5	862 ± 10	41 ± 8	–	–
	1	53 ± 25	626 ± 45	19 ± 2	27	53
	4	133 ± 19	599 ± 30	17 ± 2	31	58
	7	144 ± 19	646 ± 64	19 ± 7	25	53
	14	132 ± 4	574 ± 18	17 ± 3	33	59
AM ∥	0	5.5	1007	32	–	–
	1	105 ± 18	882 ± 26	7 ± 1	12	78
	4	190 ± 18	841 ± 83	11 ± 3	16	66
	7	191 ± 16	863 ± 26	10 ± 2	14	68
	14	204 ± 16	825 ± 52	11 ± 3	18	64
AM ⊥	0	2.5	1129 ± 29	24 ± 1	–	–
	1	70.5 ± 31	809 ± 41	13 ± 1	28	46
	4	219 ± 30	831 ± 45	10 ± 1	26	57
	7	194 ± 13	842 ± 66	10 ± 3	25	59
	14	200 ± 34	787 ± 47	9 ± 5	30	63

The properties shown are the hydrogen concentration (C_H), ultimate tensile strength (σ_{UTS}), reduction of area (RA) and Hydrogen Embrittlement Index (HEI) regarding to both the UTS and RA.

Fig. 8 | Fracture behaviour of wrought Inconel 718. a non-charged and (**b**) H-charged with a duration of 14 days. Fracture surface was characterised by dimple morphology and necking formation due to high ductility with a network of different slip band systems for non-charge conditions. After H-charging the fracture surface was brittle characterised by IG cracking along the GBs.
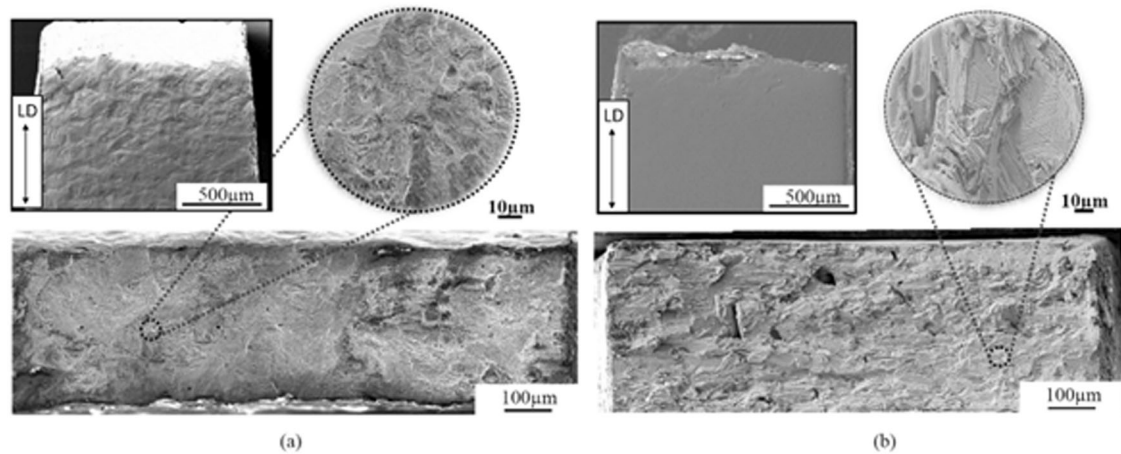
Fig. 9 | Fracture behaviour of AM Inconel 718 ‖ to BD. a non-charged and (**b**) H-charged with a duration of 14 days. Notable necking and dimples were observed on the fracture surface of the non-charged samples, with insignificant necking and intragranular cracking along the dislocation cellular boundaries, which are severally found within a single AM grain.
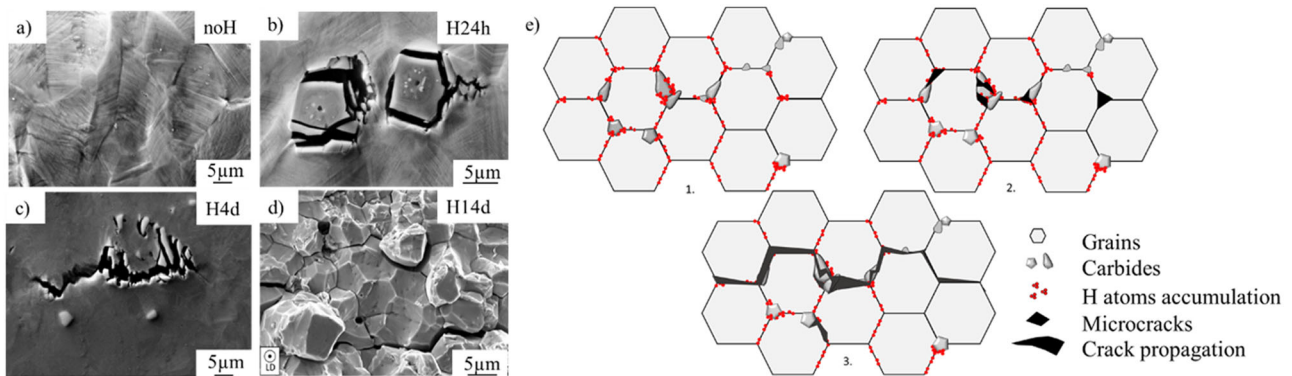

Fig. 10 | Hydrogen Embrittlement mechanism of wrought Inconel 718. a–d at different charging times. **a** Non-charged conditions, slip lines and elongated grains were visible. **b**, **c** Once charged, decohesion of matrix/carbonitride interfaces-initiated cracks. **d** The fracture surface shows the intergranular fracture of brittle behaviour. **e** It is a schematic diagram showing the crack initiation due to the decohesion and crack propagation along grain boundaries.

dislocation cell boundary in front of a very minute secondary crack. The secondary crack was very minute and on the fracture surface. Because the sample was already fractured, the residual stress surrounding the tip of this minute secondary crack on the fracture surface should be minimal. Interestingly, one month later, we observed a "delayed cracking" event, resulting in an extension of the secondary crack due to the coalescence and bridging of micro-cracks (Fig. 11a, b). This potentially suggests that hydrogen-induced decohesion caused a substantial loss in strength along the cell boundary. Such a delayed cracking event allowed us to understand how dislocation cells influence the crack initiation and propagation in the AM condition under the presence of hydrogen, hence shedding light on the mechanism responsible for the hydrogen embrittlement in AM alloys. Figure 11c shows a schematic diagram detailing the hydrogen embrittlement mechanism in AM Inconel 718: hydrogen diffuses and is trapped along cellular boundaries, which are rich in Laves phase and dislocations, significantly lowering their cohesive strength, initiating microcracks at the cellular boundaries even under minimal external loads; micro-cracks eventually bridge and coalesce to grow and propagate along the cellular boundaries, causing intra-granular fracture. Once a crack grows sufficiently long, it can propagate along grain boundaries. However, the fact that decohesion along grain boundaries occurs only once a crack attains a sufficient length implies that hydrogen-induced decohesion is more severe along cellular boundaries than grain boundaries. In addition, the intragranular fracture surface resembling the dislocation cellular microstructure (without intergranular fracture) suggests that the initiation and propagation of short cracks along dislocation cell boundaries are dominant. This highlights the pivotal role of the dislocation cellular microstructure in the hydrogen embrittlement of AM Inconel 718.

Conclusions

The present study examined the hydrogen embrittlement susceptibility of wrought and additively manufactured Inconel 718 by LPBF. This involved a detailed analysis of microstructure, hydrogen absorption and diffusivity, and mechanical behaviour with and without hydrogen charging. The following insights must be highlighted:

- **Enhanced Hydrogen Absorption:** AM Inconel 718 absorbed significantly higher amount of hydrogen (about 1.5 times) than the wrought condition. The high hydrogen absorption is hypothesised to be due to the high dislocation density present at cell walls in the AM condition. Dislocations enable pipe diffusion mechanisms, which facilitate fast diffusion of hydrogen atoms along the dislocation network, resulting in a quicker and deeper penetration of hydrogen.

- **Increased trap sites of hydrogen:** there are two types of trapping sites, one corresponding to a low binding energy attributed to lattice interstices and another trap at a higher binding energy attributed to grain boundaries for wrought and to dislocation cell boundaries for AM. A high trap density (N_t) was observed for the AM condition, corresponding to the high dislocation density associated with the cellular microstructure. The activation energy (E_a) obtained in the first
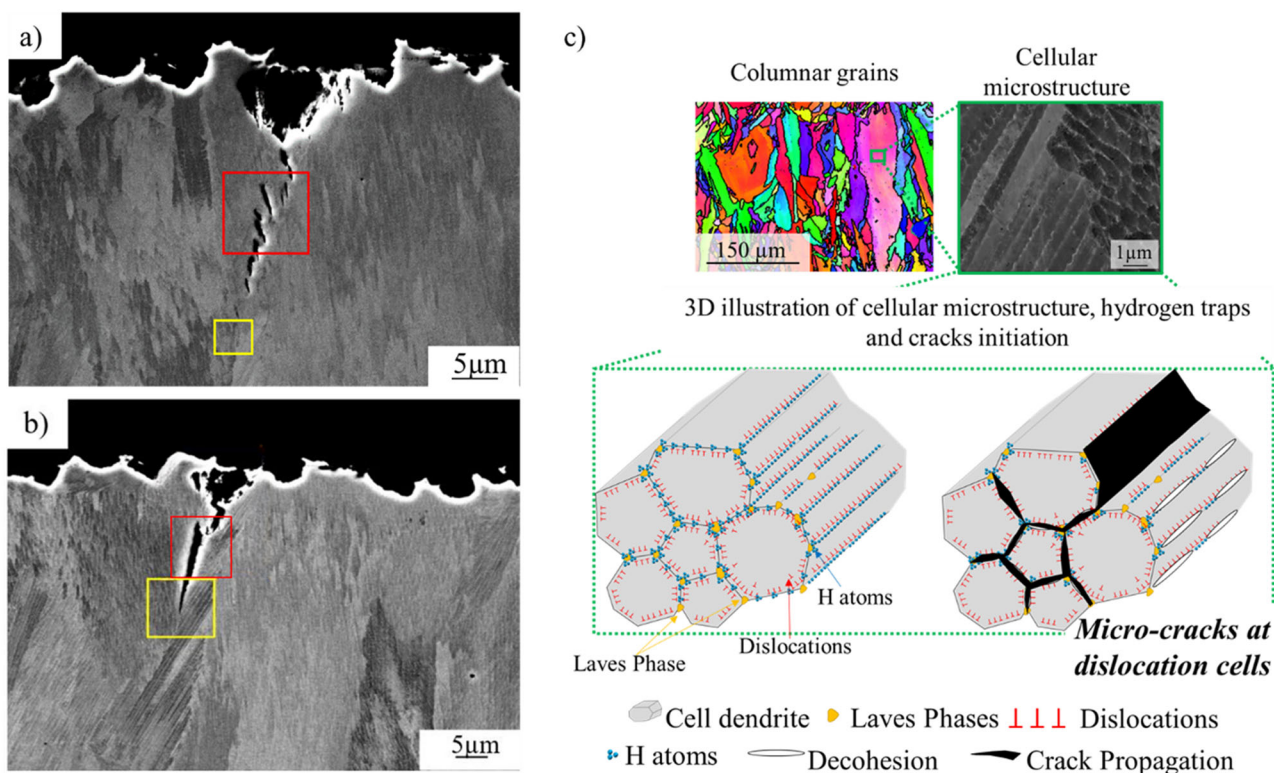
Fig. 11 | Hydrogen embrittlement mechanism of AM Inconel 718. a A minute crack secondary to the main one that caused the final fracture, (**b**) delayed cracking by micro-cracks coalescence and bridging, (**c**) a schematic diagram showing the columnar grains containing cellular microstructure and dense dislocations and Laves at the cell boundaries, and hydrogen trapping that causes the decohesion, subsequently intragranular cracks along the dislocation cell boundaries.

trapping site (44 kJ/mol) was similar to the activation energy for diffusion extracted from the Arrhenius relationship in ITDS (45.57 kJ/mol).

- **Crack initiation, growth and propagation:** Dense dislocations at cellular dendritic boundaries increase the diffusion and absorption of hydrogen in the AM condition. The preferential hydrogen trapping at dislocation cell boundaries lowers the cohesive strength, causing initiation of micro-cracks at the cell boundaries even at very low stresses. Such micro-cracks coalesce to grow cracks along the cell boundaries. In addition, the initiation and propagation of very short cracks at cell boundaries are dominant, resulting in intragranular crack propagation as observed in the AM condition compared to the intergranular crack propagation seen in the wrought condition.

In conclusion, the interaction between microstructure (particularly cellular dendrites containing dense dislocations at boundaries, i.e., dislocation cells) and hydrogen is pivotal to understanding the underlying mechanisms responsible for hydrogen embrittlement in LPBF additively manufactured Inconel 718. The gained understanding provides a solid basis for designing strategies to enhance the hydrogen resistance and mechanical reliability of AM Inconel 718 components.

Methodology
Materials
Two different manufacturing conditions of Inconel 718 were studied: a wrought Inconel 718 sheet with dimensions $400 \times 400 \times 30$ mm³ and AM Inconel 718 fabricated using a laser powder bed fusion (LPBF) Renishaw AM250 metal additive manufacturing system in the form of blocks with dimensions $40 \times 20 \times 20$ mm³. The powder feedstock was Inconel 718 provided by Höganäs with an average particle size of 17 μm. The printing parameters used were a laser power, P, of 200 W; point distance, s, of 70 μm; exposure time, t, of 70 μs; hatch spacing, h, of 90 μm; and a layer thickness, d,

of 30 μm. The scanning strategy employed was a meander (bidirectional) with an inter-layer rotation of 67°. Specimens for microstructural characterisation, tensile testing, and thermal-desorption spectroscopy (TDS) were machined from the wrought longitudinal axis and the cuboidal AM bars along the planes perpendicular (AM⊥) and parallel (AM ∥) to the building direction (BD) using electro-discharge machining (EDM). Tensile specimens were dog-bone-shaped with 19 mm of gauge length, 1.5 mm width and 0.7 mm thickness, while TDS specimens had dimensions of $10 \times 10 \times 0.7$ mm³. The preparation of samples for microstructural characterization consisted of mechanical grinding (SiC abrasive paper) up to 5 μm and polishing with 0.4 μm colloidal silica suspension. Both tensile and TDS samples were ground and polished up to 5 μm to a final thickness of 0.5 mm.

Microstructure analysis
The microstructure of the wrought and AM (both directions) Inconel 718 was analysed using ZeissTM Sigma300 scanning electron microscope (SEM) and Zeiss Auriga Cross Beam equipped with a high-resolution Bruker e-FlashHR electron backscattered diffraction (EBSD) detector. Elemental maps for the matrix composition and precipitates of interested areas were acquired with the equipped energy dispersive spectroscopy (EDS) detector. EBSD scans were conducted under an acceleration voltage of 20 kV and a step size between 0.5 and 1 μm. EBSD data was post-processed using Bruker ESPRIT 2.1 software. The geometrically necessary dislocations (GNDs) maps were calculated from the EBSD data using the mathematical framework on MTEX code, which is based on Pantleon's study[91]. Finally, the porosity density of all the 3D printed builds was determined following the Archimedes method[92,93]. Porosity quantification was also conducted using an optical microscope and ImageJ post-processing software.

Hydrogen charging
Both tensile and TDS specimens were electrochemically charged with hydrogen in a three-electrode electrochemical cell with 3 wt.% NaCl solution

at 90°C to accelerate the ingress of hydrogen in the lattice of the metal. A constant cathodic current density (J_c) of 5 mA/cm^2 was applied between the samples and a Pt counter electrode, and the solution was deaerated with N throughout the charging process[94]. The electrochemical potential of the samples (vs. a Ag/AgCl reference electrode) and the pH were regularly monitored, and the solution was replaced as necessary to keep the charging conditions constant. The samples were charged for 1, 2, 4, 7, and 14 days to assess the hydrogen absorption behaviour of the alloy and determine the influence of different hydrogen concentrations on the tensile properties.

Thermal desorption spectroscopy

To measure hydrogen contents and diffusivity, thermal desorption spectroscopy (TDS) measurements were conducted in an ultra-high vacuum thermal desorption system equipped with a regularly calibrated Hidden Analytical RC PIC quadrupole mass spectrometer (detection resolution of 4.4×10^{-6} wppm/s). Following the completion of hydrogen charging, the dwell time required to achieve the vacuum levels necessary for analysis was 30 min. More details about the TDS system and the measurement procedure are provided elsewhere[67]. Two types of TDS measurements were conducted in this work:

(i) Constant heating rate tests, where the hydrogen desorption rate (wppm/s) was recorded as a function of time while heating the sample from 25 to 850 °C at 25 °C/min. The total hydrogen content introduced in the sample during cathodic charging for each charging time was calculated by integrating the desorption spectra. These tests were used to determine hydrogen absorption behaviour (hydrogen content vs. charging time) and to characterize hydrogen trapping (trap density and binding energy). The latter was conducted on saturated samples (charging time >7 days) by fitting the output of Oriani's trapping model[34]—which assumes local equilibrium between hydrogen in the lattice and the trapping sites—to the experimental TDS desorption profiles using the MATLAB App *TDS Simulator*[60].

(ii) Isothermal TDS (ITDS) experiments at different temperatures, during which the sample (charging time >7 days) is kept at a fixed temperature and hydrogen desorption rate is monitored versus time. The diffusivity at each temperature, D, was determined by fitting the output of a 1-D finite element (FE) simulation of hydrogen transport (Fick's second law) to the experimental ITDS profile, using the fitting procedure and routine for parameter optimization presented by Zafra et al.[68]. ITDS experiments were conducted at 22, 90, 200, 300 and 400 °C, allowing the Arrhenius law to be determined both for the wrought and AM conditions.

Mechanical testing

Slow Strain Rate Tensile tests (SSRT) were performed in air at room temperature on non-charged and hydrogen pre-charged samples of wrought and AM (AM⊥ and AM ∥) Inconel 718. A minimum of 3 specimens were tested per condition. The nominal strain rate was 10^{-6} s^{-1} equivalent to a crosshead speed of 0.01 mm/min. Tensile properties were determined and susceptibility to hydrogen was assessed using the Hydrogen Embrittlement Index (HEI), which represents the percentage of reduction or increase of a specific property due to the presence of internal hydrogen. Comprehensive fracture surface analysis was performed using SEM for identification of the hydrogen-triggered fracture mechanisms.

Data availability

The data supporting the conclusions are included in the article.

References

1. Calandri, M. et al. Texture and Microstructural Features at Different Length Scales in Inconel 718 Produced by Selective Laser Melting. *Materials* **12**, 1293 (2019).

2. Vieira, V., Piglione, A., Pham, M. & Primig, S. On the detailed morphological and chemical evolution of phases during laser powder bed fusion and common post-processing heat treatments of IN718. *Addit. Manuf.* **50**, 102540 (2022).

3. Demetriou, V., Robson, J. D., Preuss, M. & Morana, R. Study of the effect of hydrogen charging on the tensile properties and microstructure of four variant heat treatments of nickel alloy 718. *Int. J. Hydrog. Energy* **42**, 23856–23870 (2017).

4. Foroni, L. Improving hydrogen embrittlement resitance of precipitation hardened nickel-alloys. 2021, URL http://onepetro.org/NACECORR/proceedings-pdf/CORR21/2CORR21/D021S008R010/2446766/nace-2021-16673.pdf/1.10.

5. Jothi, S., Merzlikin, S. V., Croft, T. N., Andersson, J. & Brown, S. G. R. An investigation of micro-mechanisms in hydrogen induced cracking in nickel-based superalloy 718. *J. Alloys Compd.* **664**, 664–681 (2016).

6. Klapper, H. S., Klöwer, J., Gosheva, O. Hydrogen embrittlement: the game changing factor in the applicability of nickel alloys in oilfield technology. *Phil. Trans. R. Soc. A* **375**, 20160415 (2017).

7. Jia, Q. & Gu, D. Selective laser melting additive manufacturing of Inconel 718 superalloy parts: Densification, microstructure and properties. *J. Alloy. Compd.* **585**, 713–721 (2014).

8. Roy, S., Kumar, R., Panda, A. & Das, R. K. A brief review on machining of inconel 718. *Mater. Today Proc.* **5**, 18664–18673 (2018).

9. Kruth, J. P., Mercelis, P., Van Vaerenbergh, J., Froyen, L. & Rombouts, M. Binding mechanisms in selective laser sintering and selective laser melting. *Rapid Prototyp. J.* **11**, 26–36 (2005).

10. Carter, L. N. et al. Process optimisation of selective laser melting using energy density model for nickel based superalloys. *Mater. Sci. Technol. (U. Kingd.)* **32**, 657–661 (2016).

11. Deng, D., Peng, R. L., Brodin, H. & Moverare, J. Microstructure and mechanical properties of Inconel 718 produced by selective laser melting: Sample orientation dependence and effects of post heat treatments. *Mater. Sci. Eng. A* **713**, 294–306 (2018).

12. Carter, L. N., Attallah, M. M. & Reed, R. C. Laser powder bed fabrication of nickel-base superalloys: Influence of parameters; characterisation, quantification and mitigation of cracking. *Superalloys* **2012**, 577–586 (2012).

13. Kumar, P. et al. Influence of laser processing parameters on porosity in Inconel 718 during additive manufacturing. *Int. J. Adv. Manuf. Technol.* **103**, 1497–1507 (2019).

14. Amato, K. N. et al. Microstructures and mechanical behavior of Inconel 718 fabricated by selective laser melting. *Acta Mater.* **60**, 2229–2239 (2012).

15. Choi, J. P. et al. Densification and microstructural investigation of Inconel 718 parts fabricated by selective laser melting. *Powder Technol.* **310**, 60–66 (2017).

16. Raza, T., Andersson, J. & Svensson, L. E. Microstructure of selective laser melted alloy 718 in As-manufactured and post heat treated condition. *Procedia Manuf.* **25**, 450–458 (2018).

17. Tucho, W. M., Cuvillier, P., Sjolyst-Kverneland, A. & Hansen, V. Microstructure and hardness studies of Inconel 718 manufactured by selective laser melting before and after solution heat treatment. *Mater. Sci. Eng. A* **689**, 220–232 (2017).

18. Valdez, M., Kozuch, C., Faierson, E. J. & Jasiuk, I. Induced porosity in Super Alloy 718 through the laser additive manufacturing process: Microstructure and mechanical properties. *J. Alloy. Compd.* **725**, 757–764 (2017).

19. Luo, S. et al. Microstructural evolution and corrosion behaviors of Inconel 718 alloy produced by selective laser melting following different heat treatments. *Addit. Manuf.* **30**, 100875 (2019).

20. Lu, X., Ma, Y. & Wang, D. On the hydrogen embrittlement behavior of nickel-based alloys: Alloys 718 and 725. *Mater. Sci. Eng. A* **792**, 139785 (2020).

21. Lu, X., Ma, Y., Peng, D., Johnsen, R. & Wang, D. In situ nanomechanical characterization of hydrogen effects on nickel-

based alloy 725 under different metallurgical conditions. *J. Mater. Sci. Technol.* **135**, 156–169 (2023).

22. Harris, Z. D. et al. Elucidating the contribution of mobile hydrogen-deformation interactions to hydrogen-induced intergranular cracking in polycrystalline nickel. *Acta Mater.* **158**, 180–192 (2018).

23. Robertson, I. M. et al. Hydrogen embrittlement understood. *Metall. Mater. Trans. B* **46**, 1085–1103 (2015).

24. Lynch, S. Hydrogen embrittlement phenomena and mechanisms. *Corros. Rev.* **30**, 105–123 (2012).

25. Turnbull, A. et al. Hydrogen transport in nickel-base alloys. *Metall. Trans. A* **23**, 3231–3244 (1992).

26. Liu, L., Tanaka, K., Hirose, A. & Kobayashi, K. F. Effects of precipitation phases on the hydrogen embrittlement sensitivity of inconel 718. *Sci. Technol. Adv. Mater.* **3**, 335–344 (2002).

27. Liu, L. et al. Study of the effect of δ phase on hydrogen embrittlement of Inconel 718 by notch tensile tests. *Corros. Sci.* **47**, 355–367 (2005).

28. Tarzimoghadam, Z., Ponge, D., Klöwer, J. & Raabe, D. Hydrogen-assisted failure in Ni-based superalloy 718 studied under in situ hydrogen charging: The role of localized deformation in crack propagation. *Acta Mater.* **128**, 365–374 (2017).

29. Galliano, F. et al. Effect of trapping and temperature on the hydrogen embrittlement susceptibility of alloy 718. *Mater. Sci. Eng. A* **611**, 370–382 (2014).

30. Tarzimoghadam, Z. et al. Multi-scale and spatially resolved hydrogen mapping in a Ni-Nb model alloy reveals the role of the δ phase in hydrogen embrittlement of alloy 718. *Acta Mater.* **109**, 69–81 (2016).

31. Martin, M. L., Somerday, B. P., Ritchie, R. O., Sofronis, P. & Robertson, I. M. Hydrogen-induced intergranular failure in nickel revisited. *Acta Mater.* **60**, 2739–2745 (2012).

32. Obasi, G. C. et al. Effect of microstructure and alloy chemistry on hydrogen embrittlement of precipitation-hardened Ni-based alloys. *Metall. Mater. Trans. A* **49**, 1167–1181 (2018).

33. Zhang, Z., Obasis, G., Morana, R. & Preuss, M. Hydrogen assisted crack initiation and propagation in a nickel-based superalloy. *Acta Mater.* **113**, 272–283 (2016).

34. Oriani, R. A. The diffusion and trapping of hydrogen in steel. *Acta Metall.* **18**, 147–157 (1970).

35. Popov, B. N. Hydrogen permeation and hydrogen-induced cracking. Corrosion Engineering. 27–364 https://doi.org/10.1016/b978-0-444-62722-3.00008-2 (2015).

36. Martínez-Pañeda, E., Niordson, C. F. & Gangloff, R. P. Strain gradient plasticity-based modeling of hydrogen environment assisted cracking. *Acta Mater.* **117**, 321–332 (2016).

37. Li, X., Zhang, J., Akiyama, E., Fu, Q. & Li, Q. Hydrogen embrittlement behavior of Inconel 718 alloy at room temperature. *J. Mater. Sci. Technol.* **35**, 499–502 (2019).

38. Fu, Z. et al. Effects of hydrogen and load frequency on the fatigue crack propagation behavior of selective laser melted Inconel 718 alloy. *Int. J. Fatigue* **160**, 106848 (2022).

39. Badrak, R. et al. Characterization of direct metal laser sintered Alloy 718 in the as-fabricated and heat treated condition. Corrosion 2018, 11297, NACE International (2018).

40. Cao, L., Thodla, R. & Li, X. Hydrogen embrittlement of additively manufactured Inconel 718. In *NACE - Int. Corros. Conf. Ser.* 1–15 (2019).

41. Hesketh, J., McClelland, N., Zhang, Y., Green, C. & Turnbull, A. Influence of additive manufacturing by laser powder bed fusion on the susceptibility of Alloy 718 to hydrogen embrittlement. *Corros. Eng. Sci. Technol.* **56**, 565–574 (2021).

42. Lee, D., Zhao, Y., Yeol, S., Ponge, D. & Jägle, E. A. Hydrogen-assisted failure in Inconel 718 fabricated by laser powder b e d fusion: The role of solidification substructure in the embrittlement. *Scr. Mater.* **207**, 114308 (2022).

43. Yoo, J. et al. Investigation of hydrogen embrittlement properties of Ni-based alloy 718 fabricated via laser powder bed fusion. *Int. J. Hydrog. Energy* **47**, 18892–18910 (2022).

44. Xu, J. et al. Hydrogen embrittlement behavior of selective laser-melted Inconel 718 alloy. *J. Mater. Res. Technol.* **23**, 359–369 (2023).

45. Maksimkin, I. P. et al. Effect of hydrogen on the structure and mechanical properties of 316L steel and inconel 718 alloy processed by selective laser melting. *Materials* **15**, 4806 (2022).

46. Pham, M.-S., Dovgyy, B., Hooper, P. A., Gourlay, C. M. & Piglione, A. The role of side-branching in microstructure development in laser powder-bed fusion. *Nat. Commun.* **11**, 749 (2020).

47. Piglione, A. et al. On the constitutive relationship between solidification cells and the fatigue behaviour of IN718 fabricated by laser powder bed fusion. *Addit. Manuf.* **47**, 102347 (2021).

48. Pei, C., Shi, D., Yuan, H. & Li, H. Assessment of mechanical properties and fatigue performance of a selective laser melted nickel-base superalloy Inconel 718. *Mater. Sci. Eng. A* **759**, 278–287 (2019).

49. Calandri M. Inconel 718 superalloy produced through Selective Laser Melting for harsh environment applications. Thesis (2020).

50. Al-Lami, J., Dessolier, T., Pirzada, T. & Pham, M.-S. Dislocation distribution, crystallographic texture evolution and plastic inhomogeneity of Inconel 718 fabricated by laser powder-bed fusion. *Adv. Eng. Mater.* **2400524**, 1–13 (2024).

51. Chlebus, E., Gruber, K., Kuźnicka, B., Kurzac, J. & Kurzynowski, T. Effect of heat treatment on the microstructure and mechanical properties of Inconel 718 processed by selective laser melting. *Mater. Sci. Eng. A* **639**, 647–655 (2015).

52. Zhu, Z. G. et al. Hierarchical microstructure and strengthening mechanisms of a CoCrFeNiMn high entropy alloy additively manufactured by selective laser melting. *Scr. Mater.* **154**, 20–24 (2018).

53. Wan, H. Y., Zhou, Z. J., Li, C. P., Chen, G. F. & Zhang, G. P. Effect of scanning strategy on grain structure and crystallographic texture of Inconel 718 processed by selective laser melting. *J. Mater. Sci. Technol.* **34**, 1799–1804 (2018).

54. Reed, R. C. The superalloys: Fundamentals and applications. (Cambridge University Press, 2008). https://doi.org/10.1017/CBO9780511541285.

55. Yang, H., Meng, L., Luo, S. & Wang, Z. Microstructural evolution and mechanical performances of selective laser melting Inconel 718 from low to high laser power. *J. Alloy. Compd.* **828**, 154473 (2020).

56. Gallmeyer, T. G. et al. Knowledge of process-structure-property relationships to engineer better heat treatments for laser powder bed fusion additive manufactured Inconel 718. *Addit. Manuf.* **31**, 100977 (2020).

57. Zhang, D., Niu, W., Cao, X. & Liu, Z. Effect of standard heat treatment on the microstructure and mechanical properties of selective laser melting manufactured Inconel 718 superalloy. *Mater. Sci. Eng. A* **644**, 32–40 (2015).

58. Dovgyy, B., Piglione, A., Hooper, P. A. & Pham, M. S. Comprehensive assessment of the printability of CoNiCrFeMn in Laser Powder Bed Fusion. *Mater. Des.* **194**, 108845 (2020).

59. McNabb, P. K. & Foster, A. A new analysis of diffusion of hydrogen in iron and ferritic steels. *Trans. Metall. Soc. AIME* **3**, 618 (1963).

60. García-Macías, E., Harris, Z., Martínez-Pañeda, E. TDS Simulator: A MATLAB App to model temperature-programmed hydrogen desorption (submitted), (n.d.).

61. Choo, W. Y. & Lee, J. Y. Thermal analysis of trapped hydrogen in pure iron. *Metall. Trans. A* **13**, 135–140 (1982).

62. Wei, F. G., Enomoto, M. & Tsuzaki, K. Applicability of the Kissinger's formula and comparison with the McNabb–Foster model in simulation of thermal desorption spectrum. *Comput. Mater. Sci.* **51**, 322–330 (2012).

63. Drexler, A., Vandewalle, L., Depover, T., Verbeken, K. & Domitner, J. Critical verification of the Kissinger theory to evaluate thermal desorption spectra. *Int. J. Hydrog. Energy* **46**, 39590–39606 (2021).

64. Díaz, A., Cuesta, I. I., Martínez-Pañeda, E. & Alegre, J. M. Influence of charging conditions on simulated temperature-programmed desorption for hydrogen in metals. *Int. J. Hydrog. Energy* **45**, 23704–23720 (2020).

65. Lee, S. M. & Lee, J. Y. The trapping and transport phenomena of hydrogen in nickel. *Metall. Trans. A* **17**, 181–187 (1986).

66. Robertson, W. M. Hydrogen Permeation and Diffusion in Inconel 718 and Incoloy 903. *Met. Trans. A* **8**, 1709–1712 (1977).

67. Zafra, A., Harris, Z., Sun, C. & Martínez-Pañeda, E. Comparison of hydrogen diffusivities measured by electrochemical permeation and temperature-programmed desorption in cold-rolled pure iron. *J. Nat. Gas. Sci. Eng.* **98**, 104365 (2022).

68. Zafra, A., Harris, Z., Korec, E. & Martínez-Pañeda, E. On the relative efficacy of electropermeation and isothermal desorption approaches for measuring hydrogen diffusivity. *Int. J. Hydrog. Energy* **48**, 1218–1233 (2023).

69. Yoo, Y. S. J., Book, T. A., Sangid, M. D. & Kacher, J. Identifying strain localization and dislocation processes in fatigued Inconel 718 manufactured from selective laser melting. *Mater. Sci. Eng. A* **724**, 444–451 (2018).

70. Liu, L. et al. Dislocation network in additive manufactured steel breaks strength–ductility trade-off. *Mater. Today* **21**, 354–361 (2018).

71. Chen, Y. S. et al. Direct observation of individual hydrogen atoms at trapping sites in a ferritic steel. *Science* **355**, 1196–1199 (2017).

72. Zhang, Z., Moore, K. L., McMahon, G., Morana, R. & Preuss, M. On the role of precipitates in hydrogen trapping and hydrogen embrittlement of a nickel-based superalloy. *Corros. Sci.* **146**, 58–69 (2019).

73. Takahashi, J., Kawakami, K., Kobayashi, Y. & Tarui, T. The first direct observation of hydrogen trapping sites in TiC precipitation-hardening steel through atom probe tomography. *Scr. Mater.* **63**, 261–264 (2010).

74. Lu, X., Depover, T. & Johnsen, R. Evaluation of hydrogen diffusion and trapping in nickel Alloy 625 by thermal desorption spectroscopy. *Int. J. Hydrog. Energy* **47**, 31673–31683 (2022).

75. Young, G. A. & Scully, J. R. Evidence that carbide precipitation produces hydrogen traps in Ni-17Cr-8Fe alloys. *Scr. Mater.* **36**, 713–719 (1997).

76. Zhou, Z. et al. The dependence of hydrogen embrittlement on hydrogen transport in selective laser melted 304L stainless steel. *Int. J. Hydrog. Energy* **46**, 16153–16163 (2021).

77. Zhang, H.-Y. et al. The Significant role of high-density dislocation cellular structure in improving the hydrogen embrittlement resistance of 304 austenitic stainless steel produced by laser selective melting, *SSRN Electron. J.* https://doi.org/10.2139/ssrn.4247018 (2022).

78. Álvarez, G., Harris, Z., Wada, K., Rodríguez, C. & Martínez-Pañeda, E. Hydrogen embrittlement susceptibility of additively manufactured 316L stainless steel: Influence of post-processing, printing direction, temperature and pre-straining. *Addit. Manuf.* **78**, 103834 (2023).

79. Love, G. R. Dislocation pipe diffusion. *Acta Metall.* **12**, 731–737 (1964).

80. Oudriss, A. et al. Grain size and grain-boundary effects on diffusion and trapping of hydrogen in pure nickel. *Acta Mater.* **60**, 6814–6828 (2012).

81. Lin, J. et al. Hydrogen permeation behavior and hydrogen-induced defects in 316L stainless steels manufactured by additive manufacturing. *Mater. Chem. Phys.* **250**, 123038 (2020).

82. Kagay, B., Findley, K., Coryell, S. & McCoy, S. Comparison of hydrogen embrittlement testing methods of UNS N07718. *NACE Int. Corros. Conf. Ser.* 1–21 https://www.osti.gov/servlets/purl/1771049 (2021).

83. Fournier, L., Delafosse, D. & Magnin, T. Cathodic hydrogen embrittlement in alloy 718. *Mater. Sci. Eng. A* **269**, 111–119 (1999).

84. Louthan, M. R. & Caskey, G. R. Hydrogen transport and embrittlement in structural metals. *Int. J. Hydrog. Energy* **1**, 291–305 (1976).

85. Hicks, P. D. & Altstetter, C. J. Hydrogen-enhanced cracking of superalloys. *Metall. Trans. A* **23**, 237–249 (1992).

86. Aiello, F. et al. Hydrogen diffusivity and tensile properties degradation in SLMed Inconel 718. *IOP Conf. Ser. Mater. Sci. Eng.* **1214**, 012002 (2022).

87. Lee, D. H., Zhao, Y., Lee, S. Y., Ponge, D. & Jägle, E. A. Hydrogen-assisted failure in Inconel 718 fabricated by laser powder bed fusion: The role of solidification substructure in the embrittlement. *Scr. Mater.* **207**, 114308 (2022).

88. Hicks, P. D. & Altstetter, C. J. Hydrogen-enhanced cracking of superalloys. *Metall. Trans. A* **23**, 237–249 (1992).

89. Kimura, A. & birnbaum, H. K. On the kinetics of intergranular embrittlement of nickel by hydrogen transport from the external surface. *Scr. Metall.* **21**, 219–222 (1987).

90. West, A. J. & Louthan, M. R. Dislocation transport and hydrogen embrittlement. *Metall. Trans. A* **10**, 1675–1682 (1979).

91. Pantleon, W. Resolving the geometrically necessary dislocation content by conventional electron backscattering diffraction. *Scr. Mater.* **58**, 994–997 (2008).

92. Kumar, S. Selective Laser Sintering/Melting, Elsevier, 2014. https://doi.org/10.1016/B978-0-08-096532-1.01003-7.

93. DebRoy, T. et al. Additive manufacturing of metallic components—Process, structure and properties. *Prog. Mater. Sci.* **92**, 112–224 (2018).

94. Cupertino-Malheiros, L., Duportal, M., Hageman, T., Zafra, A., & Martínez-Pañeda, E. Hydrogen uptake kinetics of cathodic polarized metals in aqueous electrolytes. *Corrosion Science* **231**, 111959 (2024).

95. Xu, J., Sun, X. K., Liu, Q. Q. & Chen, W. X. Hydrogen permeation behavior in IN718 and GH761 superalloys. *Metall. Mater. Trans. A* **25**, 539–544 (1994).

Acknowledgements

Author contributions

C-T.S.M.: Conceptualization, methodology, investigation, visualisation, Formal analysis, Writing—original draft. A.Z.: Investigation, Analysis, Writing—review and editing. E.M.P.: Supervision, Software, Resources, Writing—review & editing. P.S.: Resources. R.M.: Supervision, Resources. M.-S.P.: Supervision, Resources, Writing—review & editing.

Competing interests

The authors declare no competing interests.

Inclusion & Ethics approval

The authors declare that they have abided by the publication inclusion and ethics and state that this work is original and has not been used for publication anywhere before.

Additional information

Correspondence and requests for materials should be addressed to Claudia-Tatiana Santos Maldonado or Minh-Son Pham.

Peer review information *Communications Materials* thanks Wen Chen, Minsheng Huang and the other anonymous, reviewer(s) for their contribution to the peer review of this work. Primary Handling Editors: Xiaoyan Li and John Plummer.

Reprints and permissions information is available at http://www.nature.com/reprints

Publisher's note Springer Nature remains neutral with regard to jurisdictional claims in published maps and institutional affiliations.